Landslides on Charon

Chloe B. Beddingfield[a,b], Ross A. Beyer[a,b], Kelsi N. Singer[c], William B. McKinnon[d], Kirby Runyon[e], Will Grundy[f], S. Alan Stern[c], Veronica Bray[h], Rajani Dhingra[i], Jeffrey M. Moore[b], K. Ennico[b], C. B. Olkin[c], Paul Schenk[j], John R. Spencer[c], H. A. Weaver[e], L. A. Young[c], and the New Horizons Team

[a]*Sagan Center at the SETI Institute*
[b]*NASA Ames Research Center*
[c]*Southwest Research Institute, Boulder*
[d]*Washington University in St. Louis*
[e]*Johns Hopkins University Applied Physics Laboratory*
[f]*Lowell Observatory*
[g]*University of California, Santa Cruz*
[h]*University of Arizona*
[i]*University of Idaho*
[j]*Lunar and Planetary Institute*

Abstract

We investigated five large landslides identified in the Serenity Chasma region of Charon. The identification of these landslides involved a search for these features in images taken by cameras onboard the New Horizons spacecraft. Various landslide properties were analyzed based on their morphologies using a digital terrain model of the region. We found that landslides are confined to the walls of the large normal fault scarps that make up Serenity Chasma. Based on extensive landslide runout lengths (L) relative to their drop heights (H), we classified these features as long-runout landslides. By analyzing their geometries, we estimated the friction coefficients of the landslide material (H/L) to be between 0.15 to 0.31 and the runout efficiencies (L/H) to be between 3.2 and 6.8. We also estimated that the specific energy released during landslide motion ranged from 0.8 to 1.3 kJ kg^{-1}. These amounts of energy were too low to have generated significant melt around landslide particles.

A version of this paper was published in *Icarus*, copyright © 2019 Elsevier, Inc. For more information about the details, see the Appendix on page 13.

---

1. Introduction

Landslide morphologies provide critical information about the material properties and degradational histories of planetary surfaces. Landslides occur when a slope undergoes failure, creating a massive movement of material from the slope wall, which then settles at the base of the slope at or below the angle of repose (e.g. Blackwelder, 1928; Bart et al., 2011). During a landslide event, a concave alcove with freshly exposed scarp faces will form in response to the removal of material along the face of the slope.

The material making up a landslide deposit often exhibits a different texture relative to the surrounding terrain (e.g. Moore et al., 1999; Singer et al., 2012). For example, this texture may appear smoother than the surrounding terrain if the landslide consists of unconsolidated material. Alternatively, the material may instead appear more blocky than the surrounding terrain if the landslide material is made up of more rocky and consolidated materials. In both cases, the landslide deposit exhibits a lower cratering density than the surrounding terrain, and may overprint features (i.e., craters, faults, fluvial channels, other landslide deposits, etc.) (Smith et al., 1989; Moore et al., 1996, 1999; Pappalardo et al., 1997; Prockter et al., 1998; Head et al., 1999; Chuang and Greeley, 2000; Singer et al., 2012; Beddingfield et al., 2015).

Landslide deposits exhibit lobate tongue-shaped fronts and lateral landslide margins (e.g. Singer et al., 2012). On Earth, natural landslide triggering mechanisms include volumetric expansion of the material due to freeze-thaw, increases in pore pressure, loss of subsurface material, seismic forces from impact events, volcanic eruptions, or earthquakes. However, on airless icy bodies, the triggering mechanisms for these landslide features are most likely seismic activity generated by impact events, tectonism, or volcanism.

We performed a search for landslides in images from the New Horizons (Stern et al., 2015) Long-Range Reconnaissance Imager (LORRI, Cheng et al., 2008) and the Multi-spectral Visible Imaging Camera (MVIC) on the Ralph instrument (Reuter et al., 2008), to identify mass wasting features on the surface of Charon. Non-encounter hemisphere images, shown in Beyer et al. (2017b), are not high enough in resolution to identify landslide features, if these features exist. However, the majority of the encounter hemisphere of Charon was captured at 1 km/pixel or higher, with the highest resolution LORRI observation at 157 m/pixel (Schenk et al., 2018). In this work we identified landslides in the region of Serenity Chasma and estimated physical properties of these features.

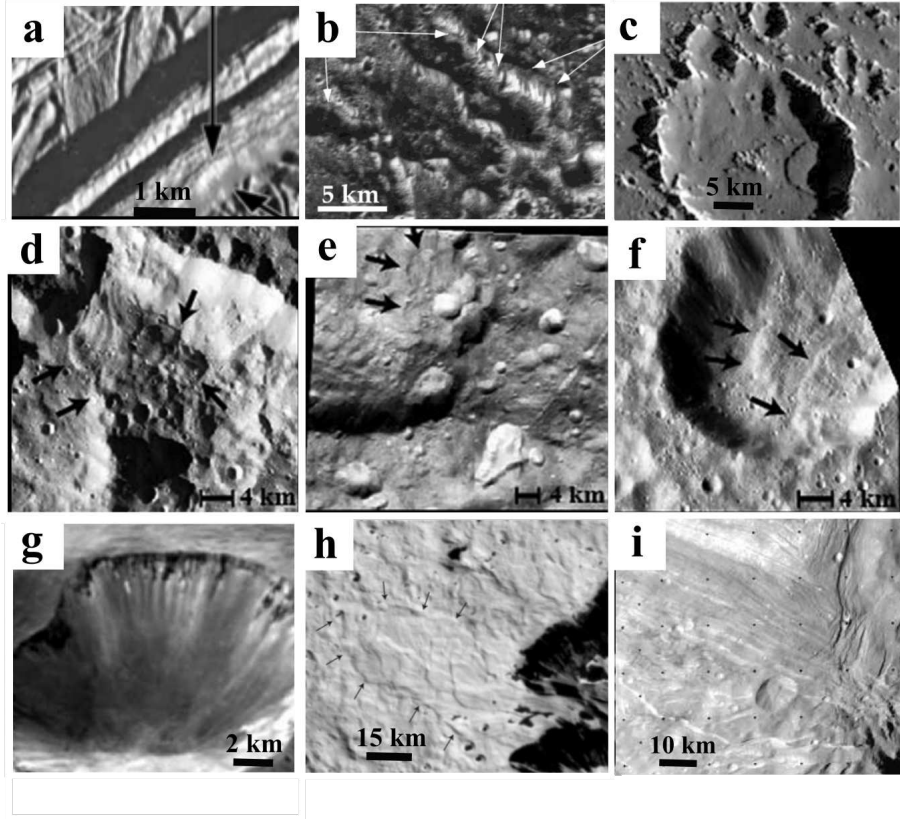*Email address:* chloe.b.beddingfield@nasa.gov (Chloe B. Beddingfield)

Figure 1: Landslides on icy bodies throughout the outer solar system. a) Subtle debris slopes on Europa. Modified figure from Moore et al. (1999). b) Low albedo streaks on Ganymede. Modified figure from Prockter et al. (1998). c) Single lobe landslide on Callisto. Modified figure from Moore et al. (1999). d) Multiple lobe landslide on Rhea. Modified figure from Beddingfield et al. (2015). e) Landslide with multiple lobes on Tethys. Modified figure from Beddingfield et al. (2015). f) Multiple lobe landslide on Dione. Modified figure from Beddingfield et al. (2015). g) Low albedo streaks on Phoebe. Modified figure from Porco et al. (2005). h) Multiple lobe landslide on Iapetus. Modified figure from Singer et al. (2012). i) Low albedo streaks on Miranda along the impact crater walls. Voyager 2 ISS image c2684611.

2. Mass Wasting Features on Icy Bodies

Various forms of mass wasting features have been identified on airless icy bodies in the jovian (e.g. Moore et al., 1999, 1996; Prockter et al., 1998; Head et al., 1999; Chuang and Greeley, 2000), saturnian (Singer et al., 2012; Beddingfield et al., 2015), uranian (Pappalardo et al., 1997), and neptunian (Smith et al., 1989; Moore et al., 1996) systems. The morphologies and albedos of icy body mass wasting features tend to vary from body to body. For example, in the jovian system, Europa exhibits subtle mass wasting features in the form of accumulations of debris at the bases of slopes (Figure 1a and e.g. Moore et al.,

3

1999, 1996; Head et al., 1999). As discussed in Moore et al. (1999), these deposits are relatively small, and extend no more than 1 km from the bases of their associated slopes. These small features are only visible in Galileo Solid State Imaging (SSI) experiment images with ground scales better than 30 m/pixel. The particles within these blocks are generally below the resolution of the available images. However, blocks of a few 100 m in diameter are visible in some locations.

Ganymede also exhibits mass wasting features that include dark streaks on slopes that widen at the slope bases (Figure 1b, Prockter et al., 1998; Pappalardo et al., 1998; Moore et al., 1999). These features exhibit lobe-shaped morphologies at the bases of their associated slopes. Callisto exhibits debris avalanches that display single lobe morphologies and smooth surfaces (Figure 1c, Chuang et al., 1999; Moore et al., 1999; Chuang and Greeley, 2000). As discussed in Moore et al. (1999), these lobes exhibit low albedos, are estimated to be 50 m to 100 m thick, and display relatively short runout distances (measured from the scarps' tops to the distal flow edges) compared to terrestrial subaerial mass movements on Earth, Venus, and Mars. Callisto's debris aprons may exhibit short runout lengths due to gravitational effects on the material's yield strength, the lack of pore pressure from liquid or vapor, or the lack of available loose material (e.g. Varnes, 1958; Moore et al., 1999).

In the saturnian system, Rhea exhibits some mass wasting features at the bases of impact crater rims, visible in the highest-resolution Cassini Imaging Science Subsystem (ISS) images (Figure 1d, Singer et al., 2013; Beddingfield et al., 2015). Similar lobe-shaped features are also observable on Tethys (Figure 1e, Singer et al., 2013; Beddingfield et al., 2015), Dione (Figure 1f, Singer et al., 2012; Beddingfield et al., 2015), Phoebe (Figure 1g, Porco et al., 2005), and Iapetus (Figure 1h, Porco et al., 2005; Singer et al., 2012). Iapetus exhibits the most massive landslides on icy bodies, with large drop heights and extensive runout lengths. The lengths of these landslides are up to 80 km, and are present at the bases of slopes associated with Iapetus' equatorial ridge and crater and basin rims. The landslides are found on both Iapetus' dark and bright terrains (Singer et al., 2012).

The uranian satellite Miranda exhibits mass wasting features at the bases of the large normal fault scarps that make up Arden and Inverness Coronae (Figure 1i). As discussed in Pappalardo et al. (1997), these features consist of low albedos, and their linear chutes are observable extending down the slopes of the scarps. Similar features are also present along the slopes of impact crater rims. In the neptunian system, mass wasting is thought to have contributed to the formation of the rugged cantelope terrain on Triton (Smith et al., 1989; Moore et al., 1996). Although typical mass wasting features on Triton are below the resolution of the Voyager 2 ISS images, evidence for slope recession due to mass wasting is exhibited as irregular scarps. Sublimation is thought to be the primary driver for Triton's mass wasting activity (Moore et al., 1999).

4

3. Long-Runout Landslides

Landslide characteristics can be analyzed based on their runout lengths (L) and drop heights (H). Typical terrestrial landslides display runout lengths that are at least two times their drop heights (e.g. Hayashi and Self, 1992; Iverson, 1997). However, long-runout landslides exhibit runout lengths that have been identified up to 40 times the drop height. These types of landslides have been identified on planets and moons, including icy bodies. For example, the extensive landslides on Iapetus are also the most prominent long-runout landslides found on an icy body (Singer et al., 2012).

Various formation mechanisms have been hypothesized for long-runout landslides. These mechanisms include a reduction in friction due to localized flash heating at the base of the landslide (Erismann, 1979, 1986; Goldsby and Tullis, 2011; Singer et al., 2012) and acoustic fluidization (e.g. Collins and Melosh, 2003; Melosh, 1979; Johnson et al., 2016). Friction reduction from flash heating may occur during a landslide event at the base of the landslide if a sufficient amount of energy is released during motion (e.g. De Blasio and Elverhøi, 2008; Singer et al., 2012). On Iapetus, friction reduction due to localized flash heating during landslide motion is suggested as a possible mechanism to lower the friction coefficients (H/L) and increase runout efficiencies (L/H) of the landslide material (Singer et al., 2012). As the temperature of the base of the ice approaches its melting temperature, the coefficient of friction within the landslide decreases, causing landslide material to slide farther from its source, creating the observed long-runout landslides. Because the total amount of energy expected for the falling material is not large, the heating would need to be localized flash heating along the sliding base of the landslide to be effective at raising the material temperature (e.g. Reimold, 1995). This flash heating is analogous to a similar mechanism for reducing terrestrial fault friction. On Iapetus, landslide geometries suggest that the friction coefficient is as low as 0.1 and the runout efficiencies are up to 10. Because the surface and near subsurface temperatures of Iapetus are around 75 K to 100 K, the increase in temperature close to melting is possible, based on the estimated amount of specific energy released during landslide events. However, it is unknown if the same effect would occur for icy bodies with colder surface temperatures, like Charon.

In addition, friction reduction due to acoustic fluidization has been suggested as a formation mechanism for long-runout landslides. Acoustic fluidization may occur from preferential slipping when overburden pressures within a landslide are relieved by transient variations in pressure during a single landslide event (Johnson et al., 2016; Johnson and Campbell, 2017). As summarized in Johnson et al. (2016), these variations in pressure cause volumes of material, with dimensions smaller than the acoustic wavelength, to easily move downslope during periods of low pressure. This formation mechanism has been proposed for landslides on Earth, Mars, and Iapetus.

4. Observations of Charon's Landslides

Based on visual inspection of New Horizons images, we identified landslides in Charon's Serenity Chasma region.[1] These observations were limited by the resolution of available images and lighting geometry. We identified five "prominent" landslides, which are covered by the highest resolution images and are large enough for their geometries to be measured. All of these prominent landslides overlie the largest fault scarps of Serenity Chasma. In addition to these prominent landslides, we also identified several "subtle" landslides. These subtle landslides are smaller and are not suitable for their geometries to be measured in available images. Subtle landslides are located within nearby impact craters and along a small ridge within Serenity Chasma. The surface areas of both prominent and subtle landslides are too small to detect composition anomalies relative to the surrounding terrain in available Charon composition maps (Dalle Ore et al., 2018).

Landslides were identified via the presence of features used to identify landslides on other icy bodies (e.g. Moore et al., 1999; Singer et al., 2012). These features consist of apparently smooth surfaces relative to the surrounding terrain, lobate tongue-shaped fronts, and concave alcoves. We refer to these five landslides based on their longitudinal locations. These landslides include the Longitude 1°, 9°, 16°, 19°, and 21° Landslides (Figure 2, Table 1).

To further investigate these landslides, we used a digital terrain model (DTM) covering Serenity Chasma and the QGIS software to measure their geometries. The DTM provided in Schenk et al. (2018) was used as a base. The Ames Stereo Pipeline (ASP, Beyer et al., 2017a, 2018) shape-from-shading algorithm (Alexandrov and Beyer, 2017, 2018) was applied to this base DTM to enhance the topographic resolution of features. The horizontal pixel resolution of the DTM is 400 m px^{-1}.

The south facing wall of Serenity Chasma hosts the Longitude 1°, 16°, 19°, and 21° Landslides, while the north facing wall, which covers less area, exhibits the 9° Landslide (Figure 3). Some landslides may consist of multiple overprinting lobes of material (Table 1) with the Longitude 9° Landslide exhibiting the largest number of lobes. These lobes range in thickness from 140 to 220 m near the landslide toe, and are detectable in the DTM (Figure 4). The toe thickness was measured at the locations where the topography of the landslides transitioned to the elevation of the surrounding terrain.

The vertical extent of the landslides, or the drop height, ranges from 2.8 to 6.7 km from the concave alcove along the associated fault scarp to the toe. The runout lengths range from 15.7 to 24.6 km (Figure 5). All five of these landslides exhibit long runout lengths relative to their drop heights. Therefore, we classified these features as long-runout landslides.

---

[1]Some names on Charon are now formalized and others are still informal, and follow the informal names in Moore et al. (2016) and Beyer et al. (2017b).
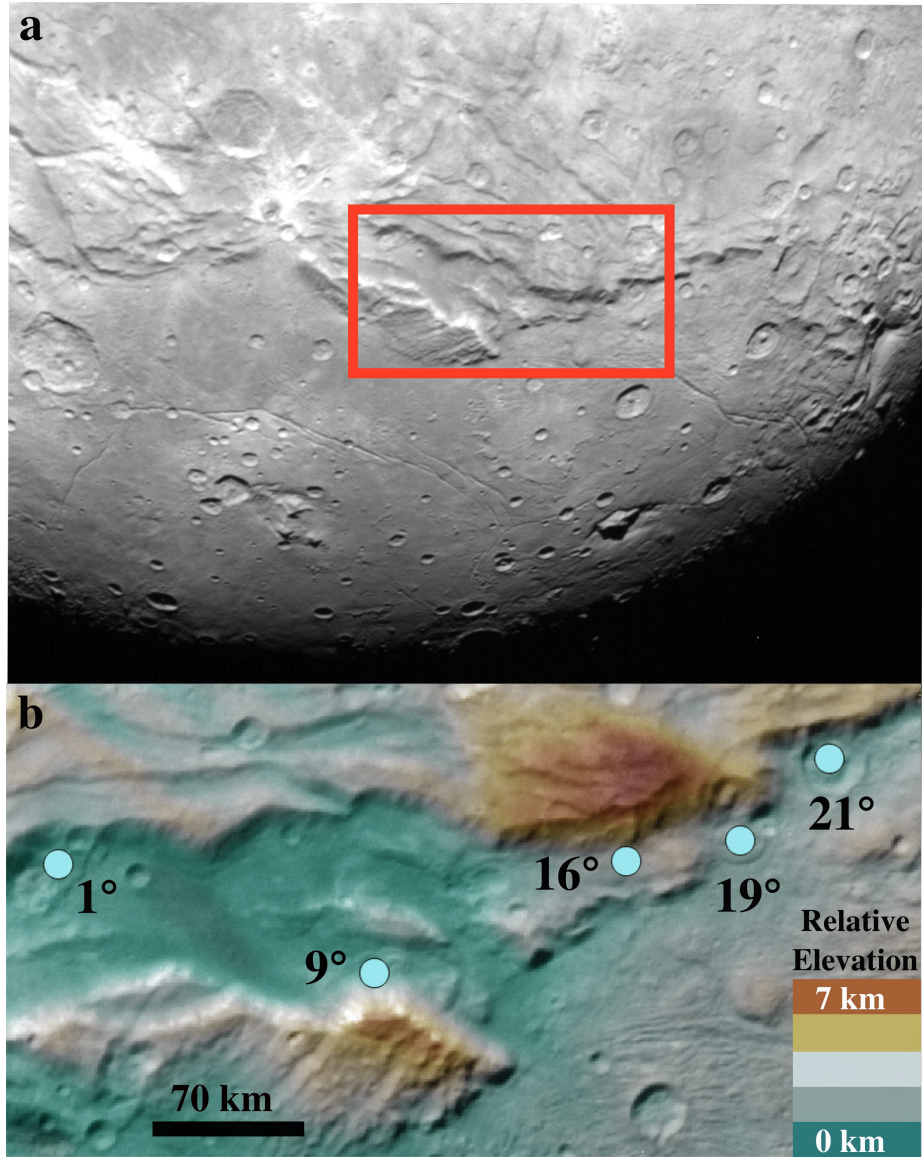
Figure 2: a) The location of the DTM shown in b. The image used is LORRI image LOR_0299171413 b) Charon's five prominent landslide locations are shown on the DTM. Each landslide was named based on its longitudinal location within Serenity Chasma. The horizontal pixel resolution of the DTM is 400 m px^{-1}. The shape-from-shading algorithm in ASP (Beyer et al., 2017a, 2018; Alexandrov and Beyer, 2017, 2018) was applied to this base DTM to enhance the topographic resolution of features. Images of the marked lobe locations are shown in Figure 3.

Table 1: Observations and measurements of Charon's landslides. As shown in Figure 6, the landslide drop height (H) was measured from the top of the scarp to the base of the scarp. The landslide runout length (L) was measured from the top of the scarp to the edge of the deposit. Because H and L are measures of the center of mass of the fall height and runout lengths respectively, our measurements provide maximum estimates for these values.

Landslide Name (Longitude)	1°	9°	16°	19°	21°
Latitude Coordinate (°)	20	17	20	21	23
Figure Reference	3a	3b	3c	3c	3c
Minimum Number of Landslide Lobes	3	4	2	1	1
Landslide Drop Height, H (km)	2.8	6.7	4.5	3.6	3.1
Landslide Runout Length, L (km)	15.7	21.5	21.3	24.6	17.0
Affected Area, Including Alcove, A (km^2)	540	640	660	270	180
Landslide Depositional Area, a (km^2)	320	450	270	150	140
Landslide Thickness Near Toe, T (m)	220	140	210	210	140
Landslide Material Friction Coefficient, μ, H/L	0.18	0.31	0.21	0.15	0.18
Landslide Runout Efficiency L/H	5.6	3.2	4.7	6.8	5.5
Specific Potential Energy, e_U (kJ kg^{-1})	0.8	1.9	1.3	1.0	0.9

5. Discussion and Analyses

5.1. Landslide Friction and Energy

The friction coefficients of cold water ice have been measured via physical deformation experiments in the laboratory (e.g. Durham et al., 1983; Beeman et al., 1988; Schulson and Fortt, 2012). Based on these laboratory results, the friction coefficient of water ice is expected to be approximately 0.55 for temperatures that range from 77 K to 115 K, and vertical normal stresses ≤ 5 MPa (e.g. Beeman et al., 1988), conditions relevant for Charon's landslides.

We analyzed Charon's landslide geometries to gather information about the friction coefficients of the landslide material. The height of the cliff face center of mass from where the landslide material is sourced, termed the drop height (H), can be compared to the center of mass of the plan-form horizontal length of a landslide from the alcove rim to the flow toe, termed the runout length (L), as seen in Figure 6. As discussed in Parez and Aharonov (2015), the friction coefficient, μ of the landslide material during movement is given by

$$\mu = \frac{H}{L}.$$

The landslide runout efficiency can be estimated from the reciprical of this value (L/H).

The estimated friction coefficients range from 0.15 to 0.31 and the runout efficiencies range from 3.2 to 6.8 for material in Charon's landslides (Table 1). These friction coefficients are low (and runout efficiencies high) compared to some terrestrial and martian landslides and those of Callisto and Rhea (see data shown in Figure 7). However, these values are comparable to those estimated
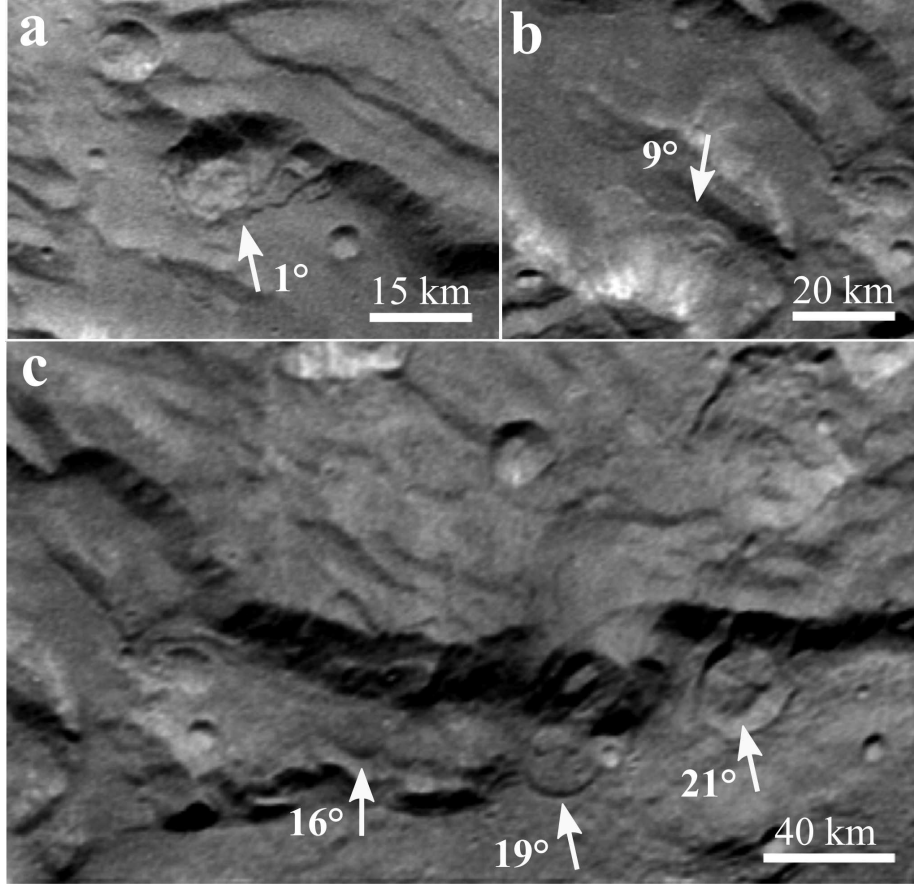
Figure 3: Landslides on Charon. All prominent landslides identified are present at the bases of large normal fault scarps that make up Serenity Chasma. a) The Longitude 1° Landslide. b) The Longitude 9° Landslide. Talus streaks are present near the top of this landslide feature. These streaks are the most prominent for the this landslide due to the illumination of the north facing Serenity Chasma scarp. c) The Longitudes 16° (left), 19° (center), and 21° (right) Landslides.

for terrestrial debris flows, rock avalanches, and pyroclastic flows on Earth and Mars (Figure 7 and e.g. Hayashi and Self, 1992; Iverson, 1997; Barnouin-Jha and Buczkowski, 2007). The friction coefficient estimates for Charon's landslides are higher than those estimated for Iapetus (Singer et al., 2012).

Additionally, we investigated if Charon's landslide events produced enough energy to create melt during their motion. Turnbull (2011) provides an equation that describes the specific energy required for melting to occur during a landslide event, E_m, and is given by
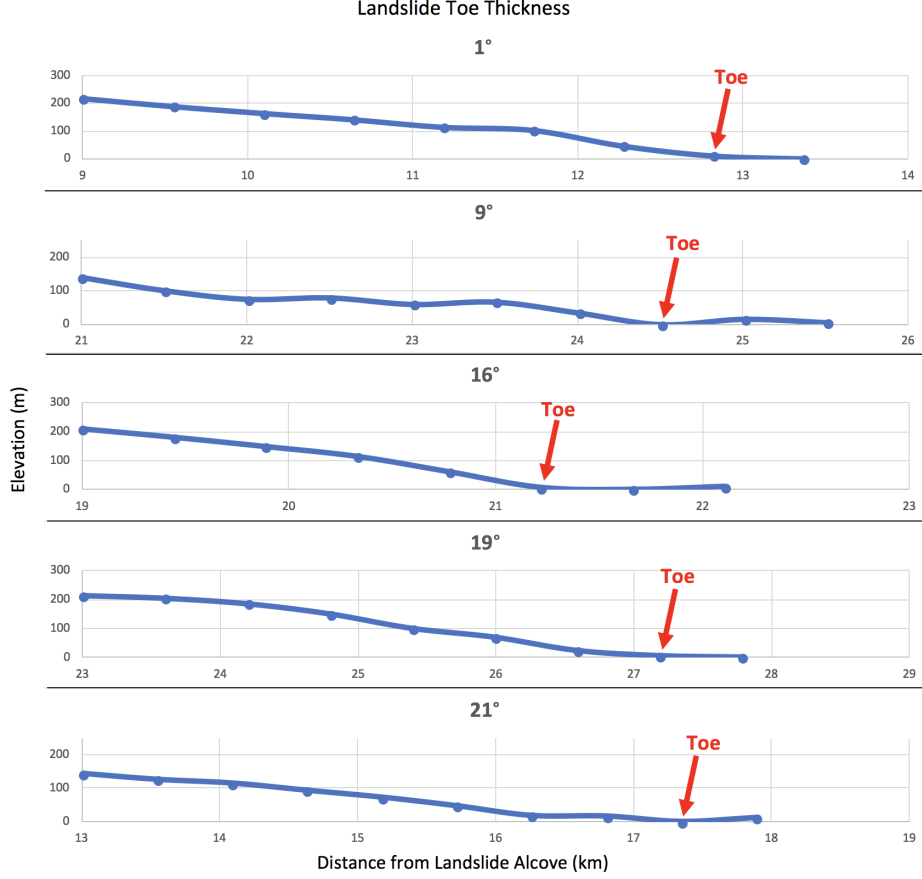
$$E_m = C_p(T_f - T_a) + \zeta$$

9

Figure 4: Landslide toe topographic profiles. These profiles show the material thickness near the toe of each landslide, and are separate measurements from those illustrated in Figure 5. The toe thickness within a few kilometers from the toe for all five prominent landslides ranges from 140 m to 220 m.

where C_p is the specific heat capacity (4.18 kJ kg^{-1} K^{-1}), T_f is the freezing temperature of ice (273.15 K), T_a is the ambient temperature on Charon (53 K), and ζ is the latent heat of fusion (334 kJ kg^{-1}) (Turnbull, 2011). Dade and Huppert (1998) provide an equation that describes the energy generated during the landslide event. The energy generated during the landslide event, E_l, is given by

$$E_l = gH$$

where g is the gravitational acceleration on Charon (0.29 m s^{-1}), and H is the landslide drop height (2.8 km to 6.7 km).

Our estimates for energy generated during landslide motion, for all five
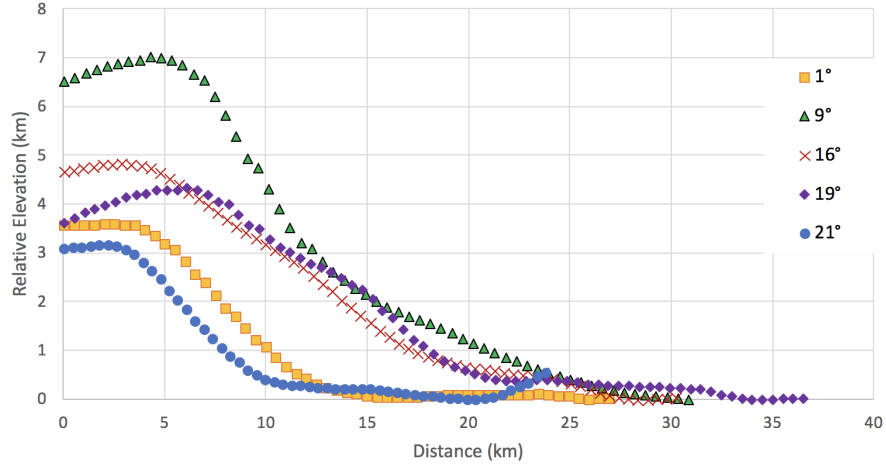
Figure 5: Charon landslide topographic profiles taken from the top of the associated normal fault scarp (left) to the toe of the landslide (right).
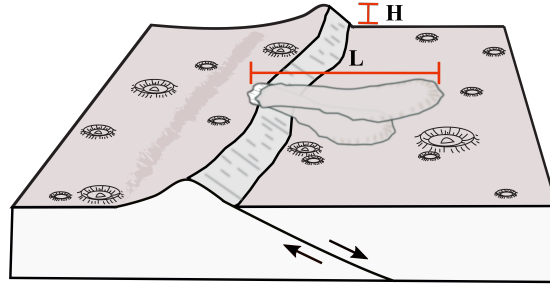

Figure 6: Landslide geometries including the drop height (H), and runout length (L). H was measured from the top of the scarp to the base of the scarp, and L was measured from the top of the scarp to the edge of the deposit.

prominent landslides, range from $0.8 \, \text{kJ} \, \text{kg}^{-1}$ to $1.9 \, \text{kJ} \, \text{kg}^{-1}$ (Table 1). However, the required specific energy required for melting to take place is $920 \, \text{kJ} \, \text{kg}^{-1}$, significantly higher that these estimated values. This energy was likely dispersed through the landslide material due to individual motion of particles during land-slide movement and spreading of the material at the slope bases.

Energy may have concentrated in areas where individual particle motion was restricted during landslide movement, allowing the ice particles to reach higher temperatures along the landslide bases. Small amounts of melt may have reduced the friction of the landslide material from the expected 0.55 found in laboratory conditions (e.g. Beeman et al., 1988) to values ranging from 0.15
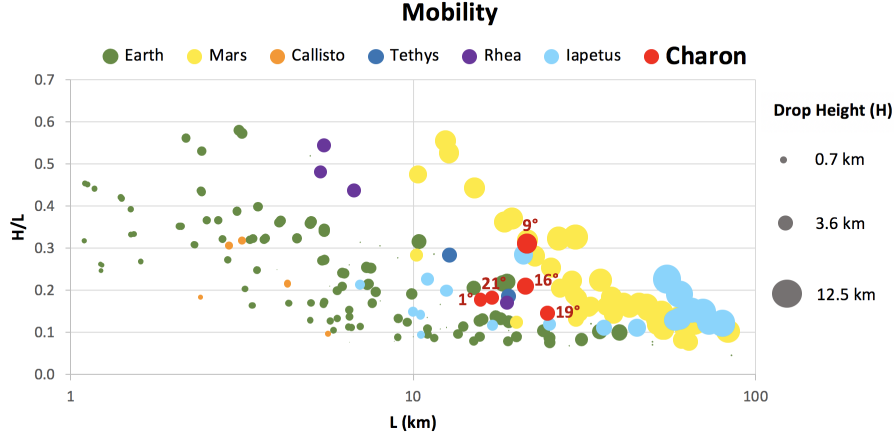
Figure 7: Illustration of landslide H/L versus L on various planetary bodies. L is taken as a proxy for landslide volume. Data collected for planetary bodies other than Charon include Earth, Mars, Tethys, Rhea, and Iapetus (e.g. Legros, 2002; McEwen, 1989; Singer et al., 2012). Terrestrial landslide data are shown for nonvolcanic and volcanic debris avalanches and pyroclastic flows (Moore and Melson, 1969; Rose et al., 1976; Davies et al., 1978; Plafker and Ericksen, 1978; Nairn and Self, 1978; Voight and Pariseau, 1978; Moore and Sisson, 1981; Ui, 1983; Siebert, 1984; Ui et al., 1986; Hoblitt, 1986; Siebert et al., 1987; Beget and Limke, 1988; Ramirez, 1988; Hayashi and Self, 1992). Similar to results found for other planetary bodies, including Earth, Mars, Callisto, Tethys, and Rhea, by (Johnson and Campbell, 2017), the runout efficiencies of Charon's landslides is inversely proportional to drop height (H).

to 0.31, estimated for Charon's landslides. In addition, the presence of ammonia hydrates within the landslide material may have also allowed the ice to more easily approach its melting temperature, since ammonia hydrates mixed with H_2O acts to reduce the melting temperature of the mixture compared to pure H_2O (Durham et al., 1993, 1998).

Small abundances of ammonia hydrates have been identified on the surface of Charon (e.g. Brown and Calvin, 2000; Dumas et al., 2001; Verbiscer et al., 2007; Grundy et al., 2016; Dalle Ore et al., 2018). Although the lifespan of ammonia hydrate is short on airless icy bodies, this constituent may be more abundant within Charon's near subsurface where it might be protected from UV radiation, perhaps within the landslide material. However, our estimates for specific energy are significantly lower than those required for significant melting to occur. Therefore, these estimates show that significant melting was unlikely during Charon's landslide events, and did not contribute to the formation of their extensive runout lengths.

6. Conclusions

We concluded that the five prominent landslides in the Serenity Chasma region of Charon are long-runout landslides, and we estimated that the friction coefficients of the landslide material during motion ranged from 0.15 to 0.30.

In addition, we estimated that the specific energy released during the landslide events was between 0.8 and 1.3 kJ kg^{-1}. This amount of energy would not have been sufficient to generate significant melt.

Appendix: Differences from the Version Published by Elsevier

As noted on the first page, this paper was originally published by Elsevier, Inc. The differences between the paper published by Elsevier and this document are essentially those of formatting. The text, figures and tables are identical. The differences are that this version provides an updated list of references, this appendix has been added, and the CC BY-NC-ND license added to apply to this version.

Elsevier, Inc. owns the copyright to the published article, the authors have created this version of the Accepted Manuscript (under the terms outlined by Elsevier, Inc.) as an excerise of one of the nonexclusive rights granted to us as authors of the work from Elsevier under the copyright transfer agreement (entitled the Journal Publishing Agreement by Elsevier).

These rights are also descibed on the "Journal author rights" page, accessed 9 August 2019, posted on the Web by Elsevier at https://www.elsevier.com/about/policies/copyright.

References

Alexandrov, O., Beyer, R.A., 2017. Multi-view shape-from-shading for planetary images with challenging illumination, in: Lunar and Planetary Science Conference, p. 3024.

Alexandrov, O., Beyer, R.A., 2018. Multiview shape-from-shading for planetary images. Earth and Space Science 5, 652–666. doi:10.1029/2018EA000390.

Barnouin-Jha, O., Buczkowski, D., 2007. Comparing the runout of fluidized ejecta on Mars with mass movements on Earth, in: Lunar and Planetary Science Conference, p. 1304.

Bart, G.D., Nickerson, R.D., Lawder, M.T., Melosh, H., 2011. Global survey of lunar regolith depths from LROC images. Icarus 215, 485–490.

Beddingfield, C.B., Burr, D.M., Dunne, W.M., 2015. Shallow normal fault slopes on Saturnian icy satellites. Journal of Geophysical Research: Planets 120, 2053–2083.

Beeman, M., Durham, W., Kirby, S., 1988. Friction of ice. Journal of Geophysical Research: Solid Earth 93, 7625–7633.

Beget, J.E., Limke, A.J., 1988. Two-dimensional kinematic and rheological modeling of the 1912 pyroclastic flow, Katmai, Alaska. Bulletin of volcanology 50, 148–160.

Beyer, R.A., Alexandrov, O., McMichael, S., 2017a. NeoGeography-Toolkit/Stereo Pipeline: Ames Stereo Pipeline 2.6.0. doi:10.5281/zenodo.581187.

Beyer, R.A., Alexandrov, O., McMichael, S., 2018. The Ames Stereo Pipeline: NASA's open source software for deriving and processing terrain data. Earth and Space Science 5, 537–548. doi:10.1029/2018ea000409.

Beyer, R.A., Nimmo, F., McKinnon, W.B., Moore, J.M., Binzel, R.P., Conrad, J.W., Cheng, A., Ennico, K., Lauer, T.R., Olkin, C.B., Robbins, S., Schenk, P., Singer, K., Spencer, J.R., Stern, S.A., Weaver, H.A., Young, L.A., Zangari, A.M., 2017b. Charon Tectonics. Icarus 287, 161–174. doi:10.1016/j.icarus.2016.12.018.

Blackwelder, E., 1928. The recognition of fault scarps. The Journal of Geology 36, 289–311.

Brown, M.E., Calvin, W.M., 2000. Evidence for crystalline water and ammonia ices on Pluto's satellite Charon. Science 287, 107–109.

Cheng, A.F., Weaver, H.A., Conard, S.J., Morgan, M.F., Barnouin-Jha, O., Boldt, J.D., Cooper, K.A., Darlington, E.H., Grey, M.P., Hayes, J.R., Kosakowski, K.E., Magee, T., Rossano, E., Sampath, D., Schlemm, C., Taylor, H.W., 2008. Long-Range Reconnaissance Imager on New Horizons. Space Science Reviews 140, 189–215. doi:10.1007/s11214-007-9271-6.

Chuang, F., Greeley, R., Moore, J., Team, G.S., et al., 1999. Callisto: Large-scale mass movements observed from the Galileo nominal mission, in: Lunar and Planetary Science Conference.

Chuang, F.C., Greeley, R., 2000. Large mass movements on Callisto. Journal of Geophysical Research: Planets 105, 20227–20244.

Collins, G.S., Melosh, H.J., 2003. Acoustic fluidization and the extraordinary mobility of sturzstroms. Journal of Geophysical Research: Solid Earth 108.

Dade, B.W., Huppert, H.E., 1998. Long-runout rockfalls. Geology 26, 803–806.

Dalle Ore, C.M., Protopapa, S., Cook, J., Grundy, W., Cruikshank, D., Verbiscer, A., Ennico, K., Olkin, C., Stern, S., Weaver, H., et al., 2018. Ices on Charon: Distribution of H_2O and NH_3 from New Horizons LEISA observations. Icarus 300, 21–32.

Davies, D.K., Quearry, M.W., Bonis, S.B., 1978. Glowing avalanches from the 1974 eruption of the volcano Fuego, Guatemala. Geological Society of America Bulletin 89, 369–384.

De Blasio, F.V., Elverhøi, A., 2008. A model for frictional melt production beneath large rock avalanches. Journal of Geophysical Research: Earth Surface 113.

Dumas, C., Terrile, R.J., Brown, R.H., Schneider, G., Smith, B.A., 2001. Hubble Space Telescope NICMOS spectroscopy of Charon's leading and trailing hemispheres. The Astronomical Journal 121, 1163.

Durham, W., Heard, H., Kirby, S., 1983. Experimental deformation of polycrystalline H_2O ice at high pressure and low temperature: Preliminary results. Journal of Geophysical Research: Solid Earth 88.

Durham, W., Kirby, S., Stern, L., 1993. Flow of ices in the ammonia-water system. Journal of Geophysical Research: Solid Earth 98, 17667–17682.

Durham, W., Kirby, S., Stern, L., 1998. Rheology of planetary ices, in: Solar system ices. Springer, pp. 63–78.

Erismann, T., 1979. Mechanisms of large landslides. Rock Mechanics 12, 15–46.

Erismann, T., 1986. Flowing, rolling, bouncing, sliding: synopsis of basic mechanisms. Acta Mechanica 64, 101–110.

Goldsby, D.L., Tullis, T.E., 2011. Flash heating leads to low frictional strength of crustal rocks at earthquake slip rates. Science 334, 216–218.

Grundy, W., Binzel, R., Buratti, B., Cook, J., Cruikshank, D., Dalle Ore, C., Earle, A., Ennico, K., Howett, C., Lunsford, A., et al., 2016. Surface compositions across Pluto and Charon. Science 351, aad9189.

Hayashi, J., Self, S., 1992. A comparison of pyroclastic flow and debris avalanche mobility. Journal of Geophysical Research: Solid Earth 97, 9063–9071.

Head, J.W., Pappalardo, R.T., Sullivan, R., 1999. Europa: Morphological characteristics of ridges and triple bands from Galileo data (E4 and E6) and assessment of a linear diapirism model. Journal of Geophysical Research: Planets 104, 24223–24236.

Hoblitt, R.P., 1986. Observations of the eruptions of July 22 and August 7, 1980, at Mount St. Helens, Washington. Technical Report. USGS. URL: http://pubs.er.usgs.gov/publication/pp1335, doi:10.3133/pp1335.

Iverson, R.M., 1997. The physics of debris flows. Reviews of geophysics 35, 245–296.

Johnson, B.C., Campbell, C.S., 2017. Drop height and volume control the mobility of long-runout landslides on the Earth and Mars. Geophysical Research Letters 44, 12091–12097.

Johnson, B.C., Campbell, C.S., Melosh, H.J., 2016. The reduction of friction in long runout landslides as an emergent phenomenon. Journal of Geophysical Research: Earth Surface 121, 881–889.

Legros, F., 2002. The mobility of long-runout landslides. Engineering Geology 63, 301–331.

McEwen, A.S., 1989. Mobility of large rock avalanches: Evidence from Valles Marineris, Mars. Geology 17, 1111–1114.

Melosh, H.J., 1979. Acoustic fluidization: A new geologic process? Journal of Geophysical Research: Solid Earth 84, 7513–7520.

Moore, J.G., Melson, W., 1969. Nuees ardentes of the 1968 eruption of Mayon volcano, Philippines. Bulletin Volcanologique 33, 600–620.

Moore, J.G., Sisson, T.W., 1981. Deposits and effects of the May 18 pyroclastic surge. US Geol. Surv. Prof. Pap 1250, 421–438.

Moore, J.M., Asphaug, E., Morrison, D., Spencer, J.R., Chapman, C.R., Bierhaus, B., Sullivan, R.J., Chuang, F.C., Klemaszewski, J.E., Greeley, R., et al., 1999. Mass movement and landform degradation on the icy Galilean satellites: Results of the Galileo nominal mission. Icarus 140, 294–312.

Moore, J.M., McKinnon, W.B., Spencer, J.R., Howard, A.D., Schenk, P.M., Beyer, R.A., Nimmo, F., Singer, K.N., Umurhan, O.M., White, O.L., et al., 2016. The geology of pluto and charon through the eyes of new horizons. Science 351, 1284–1293.

Moore, J.M., Mellon, M.T., Zent, A.P., 1996. Mass wasting and ground collapse in terrains of volatile-rich deposits as a solar system-wide geological process: The pre-Galileo view. Icarus 122, 63–78.

Nairn, I., Self, S., 1978. Explosive eruptions and pyroclastic avalanches from Ngauruhoe in February 1975. Journal of volcanology and geothermal research 3, 39–60.

Pappalardo, R.T., Head, J.W., Collins, G.C., Kirk, R.L., Neukum, G., Oberst, J., Giese, B., Greeley, R., Chapman, C.R., Helfenstein, P., et al., 1998. Grooved terrain on Ganymede: First results from Galileo high-resolution imaging. Icarus 135, 276–302.

Pappalardo, R.T., Reynolds, S.J., Greeley, R., 1997. Extensional tilt blocks on Miranda: Evidence for an upwelling origin of Arden Corona. Journal of Geophysical Research: Planets 102, 13369–13379.

Parez, S., Aharonov, E., 2015. Long runout landslides: a solution from granular mechanics. Frontiers in Physics 3, 80.

Plafker, G., Ericksen, G., 1978. Nevados Huascaran avalanches, Peru, in: Developments in Geotechnical Engineering. Elsevier. volume 14, pp. 277–314.

Porco, C., Baker, E., Barbara, J., Beurle, K., Brahic, A., Burns, J., Charnoz, S., Cooper, N., Dawson, D., Del Genio, A., et al., 2005. Cassini imaging science: Initial results on Phoebe and Iapetus. science 307, 1237–1242.

Prockter, L.M., Head, J.W., Pappalardo, R.T., Senske, D.A., Neukum, G., Wagner, R., Wolf, U., Oberst, J.O., Giese, B., Moore, J.M., et al., 1998. Dark terrain on Ganymede: Geological mapping and interpretation of Galileo Regio at high resolution. Icarus 135, 317–344.

Ramirez, C., 1988. The geology of Socompa volcano and its debris avalanche deposit, northern Chile, in: M. Philos. Thesis. Open University Milton Keynes, UK, p. 232.

Reimold, W., 1995. Pseudotachylite in impact structures—generation by friction melting and shock brecciation?: A review and discussion. Earth-Science Reviews 39, 247–265.

Reuter, D.C., Stern, S.A., Scherrer, J., Jennings, D.E., Baer, J.W., Hanley, J., Hardaway, L., Lunsford, A., McMuldroch, S., Moore, J., et al., 2008. Ralph: A visible/infrared imager for the New Horizons Pluto/Kuiper belt mission. Space Science Reviews 140, 129–154.

Rose, W.I., Pearson, T., Bonis, S., 1976. Nuee ardente eruption from the foot of a dacite lava flow, Santiaguito Volcano, Guatemala. Bulletin volcanologique 40, 23–38.

Schenk, P., Beyer, R., McKinnon, W., Moore, J., Spencer, J., White, O., Singer, K., Umurhan, O., Nimmo, F., Lauer, T., Grundy, W., Robbins, S., Stern, S., Weaver, H., Young, L., Ennico Smith, K., Olkine, C., the New Horizons Geology, Team, G.I., 2018. Breaking up is hard to do: Global cartography and topography of Pluto's mid-sized icy moon Charon from New Horizons. Icarus 315, 124–145. doi:10.1016/j.icarus.2018.06.010.

Schulson, E.M., Fortt, A.L., 2012. Friction of ice on ice. Journal of Geophysical Research: Solid Earth 117.

Siebert, L., 1984. Large volcanic debris avalanches: Characteristics of source areas, deposits, and associated eruptions. Journal of volcanology and geothermal research 22, 163–197.

Siebert, L., Glicken, H., Ui, T., 1987. Volcanic hazards from Bezymianny-and Bandai-type eruptions. Bulletin of Volcanology 49, 435–459.

Singer, K., McKinnon, W., Schenk, P., 2013. Large landslides on icy satellites: New examples from Rhea and Tethys, in: Lunar and Planetary Science Conference, p. 2955.

Singer, K.N., McKinnon, W.B., Schenk, P.M., Moore, J.M., 2012. Massive ice avalanches on Iapetus mobilized by friction reduction during flash heating. Nature Geoscience 5, 574.

Smith, B.A., Soderblom, L., Banfield, D., Basilevsky, A., Beebe, R., Bollinger, K., Boyce, J., Brahic, A., Briggs, G., Brown, R., et al., 1989. Voyager 2 at Neptune: Imaging science results. Science 246, 1422–1449.

Stern, S.A., Bagenal, F., Ennico, K., Gladstone, G., Grundy, W., McKinnon, W., Moore, J., Olkin, C., Spencer, J., Weaver, H., et al., 2015. The Pluto system: Initial results from its exploration by New Horizons. Science 350, aad1815.

Turnbull, B., 2011. Scaling laws for melting ice avalanches. Physical review letters 107, 258001.

Ui, T., 1983. Volcanic dry avalanche deposits—identification and comparison with nonvolcanic debris stream deposits. Journal of Volcanology and Geothermal Research 18, 135–150.

Ui, T., Yamamoto, H., Suzuki-Kamata, K., 1986. Characterization of debris avalanche deposits in Japan. Journal of Volcanology and Geothermal Research 29, 231–243.

Varnes, D.J., 1958. Landslide types and processes. Landslides and engineering practice 29, 20–45.

Verbiscer, A., Peterson, D., Skrutskie, M., Cushing, M., Nelson, M., Smith, J., Wilson, J., 2007. Simultaneous spatially-resolved near-infrared spectra of Pluto and Charon, in: Lunar and Planetary Science Conference, p. 2318.

Voight, B., Pariseau, W.G., 1978. Rockslides and avalanches: an introduction. Rockslides and avalanches 1.